COMMUNICATION

Check for updates

Joint tuning of nanostructured Cu-oxide morphology and local electrolyte programs high-rate CO$_2$ reduction to C$_2$H$_4$†

Yuanjie Pang, [ID] ‡[a,b] Thomas Burdyny, [ID] ‡[a] Cao-Thang Dinh,[b] Md Golam Kibria,[b] James Zhangming Fan,[b] Min Liu,[b] Edward H. Sargent*[b] and David Sinton [ID] *[a]

Electrochemical ethylene production rates are enhanced by pushing favourable local electrolyte conditions to occur at higher current densities and lower relative overpotentials. In particular the combined influences of electrode morphology and buffering on electrode pH and CO$_2$ conditions are assessed.

Electrocatalytic reduction of carbon dioxide (CO$_2$) to produce valuable carbon-based fuels and feedstocks is an important step in utilizing intermittent renewable energy.[1] As compared to promising photocatalytic CO$_2$ reduction,[2–4] the electrocatalytic approach is attractive due to its higher throughput and energy conversion efficiencies, despite requiring an external energy source. Several carbon-based compounds can currently be produced *via* the electrocatalytic CO$_2$ reduction reaction (CO$_2$RR) including carbon monoxide (CO),[5–7] methane (CH$_4$),[8] formates,[9,10] methanol,[11] and ethylene.[12,13] Among these products ethylene (C$_2$H$_4$) benefits from a large existing global market and price point compared to other one- and two-carbon products. To date, copper (Cu), Cu-based materials and N-doped carbon[14] are the only known catalysts that can produce C$_2$H$_4$ with encouraging efficiencies.

Significant research efforts have focused on increasing the Faradaic efficiency (FE) of C$_2$H$_4$ on Cu-based catalysts *via* material-based mechanisms. The use of an oxide-derived Cu catalyst has recently proven to have superior reaction kinetics for C$_2$H$_4$ production with multiple authors reporting FE's greater than 40%.[15–19] The record FE of 60%, however, belongs to a plasma-activated Cu oxide-derived surface configuration.[12] Nanostructure engineering of Cu metal offers an additional path to high C$_2$H$_4$ FE. Various surface morphologies have been devised using Cu-based catalysts including nanoparticles,[20,21] nanocubes,[13,22] and nanowires,[23,24] with the highest FE for C$_2$H$_4$ reaching 41%.

In addition to varying catalyst design, both experimental and theoretical research has pointed to the reaction environment as a primary factor in C$_2$H$_4$ selectivity on oxide-derived Cu. Most notable is the local pH at the electrode surface which varies as a function of current density and buffering capacity.[25,26] On a Cu-oxide derived catalyst a higher local pH has been shown to inhibit the surface protonation pathway of adsorbed CO towards methane, resulting in an increase in CO-CO coupling leading to C2+ product formation.[23,27] A way to locally influence local pH is confinement which has also been shown to influence selectivity with both shallow nanopores[28] and deeper micropores[29,30] enhancing C$_2$H$_4$ and ethane (C$_2$H$_6$) formation, in addition to maintaining high concentrations of reaction intermediates within the pores. Similar mass transport manipulations on the microscale were also meticulously studied in the context of CO formation where H$_2$ formation was suppressed *via* diffusional gradients, albeit at low current densities <1 mA cm^{-2}.[31] Confined structures, however, simultaneously restrict transport of CO$_2$ reagent from the bulk electrolyte limiting the use of this approach for attaining higher currents.

Despite increases in selectivity and understanding the underlying mechanisms of C$_2$H$_4$ production *via* CO$_2$RR, maximum C$_2$H$_4$ production rates under ambient conditions (1 atm, 298 K) have been limited to low partial current densities (<15 mA cm^{-2}). Reaching higher C$_2$H$_4$ partial currents requires more than increasing the mass transport of CO$_2$, however, due to competing CH$_4$ and hydrogen (H$_2$) production, both of which increase significantly with overpotential. Using a simplified supporting model and a roughened electrode Kas *et al.* began to address the entangled reaction processes by manipulating pressure and electrolyte buffering to preferentially switch selectivity between CH$_4$ and C$_2$H$_4$.[32] Interestingly the C$_2$H$_4$/CH$_4$ ratio was increased by two separate means, (i) by using low buffering concentrations to increase local pH and suppress CH$_4$ and, (ii) by oversupplying CO$_2$ using high pressure to increase CO surface coverage, promoting CO dimerization[33] and C$_2$H$_4$ formation. Similarly Varela *et al.* varied electrolyte concen-

[a]Department of Mechanical and Industrial Engineering, University of Toronto, 5 King's College Road, Toronto, Ontario, M5S 3G8, Canada. E-mail: sinton@mie.utoronto.ca
[b]Department of Electrical and Computer Engineering, University of Toronto, 35 St George Street, Toronto, Ontario, M5S 1A4, Canada.
†Electronic supplementary information (ESI) available. See DOI: 10.1039/c7gc01677h
‡These authors contributed equally to the manuscript.

tration on a mechanically polished electrode surface finding that while H_2 and CH_4 formation increase with buffering, the C_2H_4 production rate remains relatively constant indicating the increased proton availability promotes competing reactions while maintaining C_2H_4.[34] In parallel, Xiao *et al.* identified onset potentials for both C_2H_4 and CH_4 on Cu (111) at different pH values. While the onset potentials for each product were equal at a pH of 7, the onset potential for CH_4 was suppressed by ~250 mV at a pH of 12, suggesting that CO_2RR can be driven towards C2 products only over a narrow range of operating potentials.[35] These findings are similarly supported by the experimental findings of Schouten *et al.*[36] and highlight the numerous contributing factors that must be taken into account to simultaneously improve C_2H_4 selectivity and current density on oxide-derived Cu catalysts.

Here we assess the importance of varying electrode surface area, morphology and CO_2 availability in concert with electrolyte concentration to increase C_2H_4 partial current densities on oxide-derived Cu. A primary focus is to promote C_2H_4 selectivity by operating within local environments that suppress the primary competing CO_2RR product, CH_4, which both consumes CO_2 reagent and reduces overall C_2H_4 selectivity. Where possible the Cu-oxide derived electrodes should then be operated in a narrow potential window immediately after the onset of C_2H_4 production with the surrounding microenvironment at an elevated local pH. Using an updated electrochemical model accounting for surface mass transport as guidance for our experiments, we operate several electrode morphologies within the expected overpotential window for C_2H_4 production and show a shift in the peak C_2H_4 selectivity towards higher overall current densities. The impact of buffering on CO_2 availability is also addressed. Finally, the opportunities and fundamental limitations of C_2H_4 production on Cu-oxide derived catalysts in fully aqueous systems is discussed.

Results and discussion

To create electrodes with varying active surface areas but similar surface characteristics we first electrodeposited thin

Cu layers onto a cleaned Cu foil surface. Operating in galvanostatic mode with a current density of 3 A cm^{-2} thin microporous foams were formed as the result of simultaneous Cu deposition and H_2 evolution.[37] Four types of porous Cu structures were deposited using this method, with deposition durations of 2 s (Porous 1), 4 s (Porous 2), 8 s (Porous 3) and 16 s (Porous 4). A bare Cu foil surface (Flat) was also used in testing. Following the deposition process all five samples were oxidized using a wet-chemical etching technique to provide a uniformly oxidized surface (see Experimental section). SEM images of the samples after wet-oxidation can be seen in Fig. 1a–e with varying levels of roughness and porosity. The surface area of the samples with increasing deposition times was compared by plotting charging current densities *vs.* scan rates to measure the double-layer capacitance (Fig. S1†) and using under potential deposition of lead (Pb) (Fig. S2†). Both methods show an increasing trend in electrochemically-active surface area with increased deposition time in agreement with the SEM images. To confirm that the oxidation states of each of our five samples were identical to one another, X-ray photoelectron spectroscopy (XPS) measurements were performed before and after the reaction (Fig. S3†). In each case, it is found that after the reduction reaction the copper oxidation state from the wet-oxidation process was reduced. Similar to the findings of other researchers we then conclude that the formed oxide layer is reduced to bare Cu at the beginning of the CO_2 reduction process, giving an oxide-derived Cu reaction surface.[12,38–40] Further details about the electrode deposition and oxidization process can be found in the Experimental section while SEM images of each electrode as electrodeposited, after wet-oxidation and after 30 min of CO_2RR can be found in Fig. S4 of the ESI.†

Prior to CO_2 reduction we characterized the bulk mass transport properties from gas evolution on each catalyst to aid in our analysis of the experimental results (see ESI†).[41] The mass transport properties of a particular surface are important as they influence both the availability of CO_2 reagent and the energetic efficiency of the reaction. The latter is important as enhanced mass transport can reduce the overpotentials needed to reach higher current densities allowing for CH_4 to
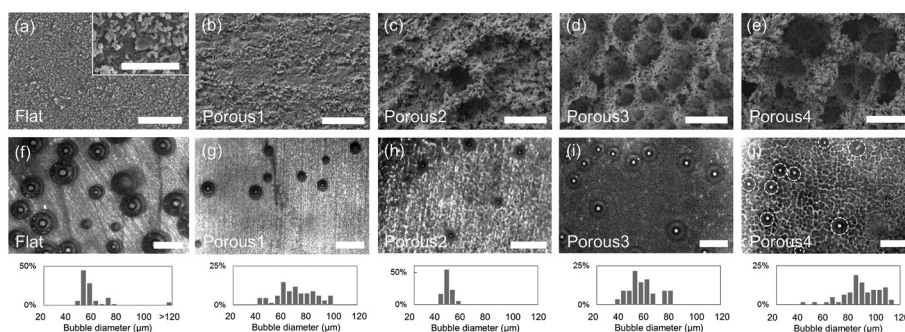

Fig. 1 (a–e) SEM Images of five different flat and electrodeposited Cu electrodes that have undergone a wet-chemical oxidation process. Scale bars are equivalent to 20 μm, inset scale bar in (a) is 3 μm. (f–j) Images of gas product bubbling during CO_2RR on various Cu electrodes taken using a dark field optical microscope. Scale bars are equivalent to 200 μm. Below each bubble image is a histogram showing the distribution of bubble diameters.
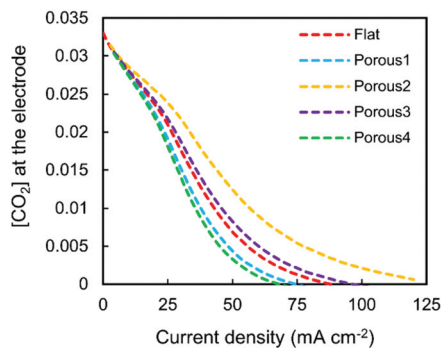
Fig. 2 Predicted local electrode CO_2 concentration using a diffusion based model and variable-diffusion thickness for five Cu-oxide derived electrodes of varying morphology in 0.1 M $KHCO_3$.

be suppressed over a larger current range during C_2H_4 production. Using a dark field microscope we observed gas evolution from each morphology and measured the diameters of the released bubbles in order to calculate the bubble-induced mass transport in each case. At current densities over 10 mA cm^{-2} bubble-induced mass transport dominates over the effects of moderately a stirred beaker resulting in a varying diffusion layer thickness that can be approximated using the bubble size distribution from a gas-evolving electrode. This addition represents the primary modeling deviation from the widely utilized model by Gupta *et al.*[25,42] The measured bubble-size distributions are shown in Fig. 1f–j in addition to

still images of the gas evolution on each structure. By pairing these results with the diffusion layer modeling aspects of other established models,[25,26,43] the local pH and CO_2 concentration at the electrode surface is approximated as a function of current density and product selectivity. Using a prescribed selectivity distribution of 50% H_2, 30% C_2H_4, 10% CH_4, 5% HCOOH and 5% EtOH the predicted mass transport kinetics of each morphology can be compared by predicting the local CO_2 concentration as a function of current density as shown in Fig. 2. From Fig. 2 the Porous 2 sample provides the greatest mass transport while the Flat, Porous 1 and Porous 4 samples result in the worst.

As a baseline for comparison to our porous samples we first performed reduction experiments on our Flat Cu sample (see Experimental section for details). The FE's of C_2H_4 for several current densities were obtained in $KHCO_3$ concentrations of 0.1 M, 0.2 M, 0.3 M and 0.5 M and are plotted in Fig. 3a. As shown in Fig. 3a and b the C_2H_4 selectivity decreases with increased buffering concentration while CH_4 selectivity increases as has been similarly demonstrated elsewhere.[32,34] It is important to note that despite a drop in C_2H_4 selectivity the overall production rate remains relatively constant (see Fig. S5†). Using our model accounting for mass transport on the flat electrode we predicted the local pH and CO_2 concentration in Fig. 3d and e using the same prescribed selectivity as in Fig. 2 and compared the results against our experimental operating voltages.

At 0.1 M $KHCO_3$ the potentials at which both CH_4 and C_2H_4 were detected is −1.1 V *vs.* reversible hydrogen electrode (RHE)
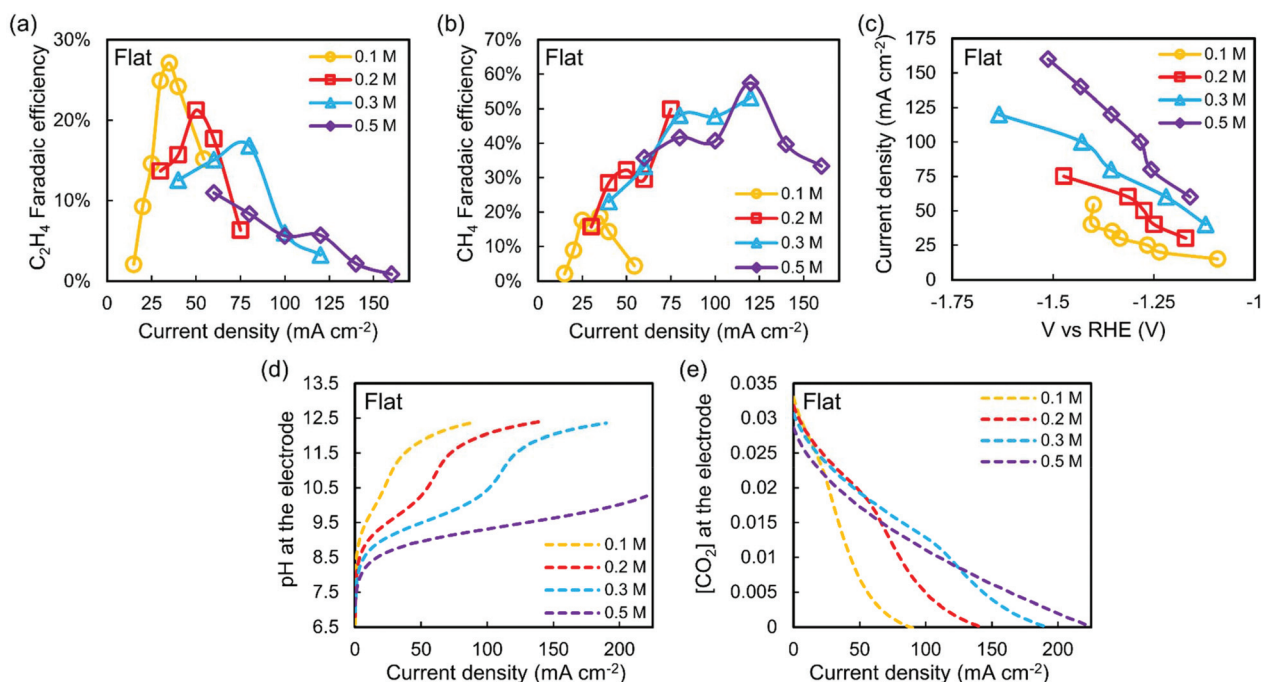

Fig. 3 (a) C_2H_4 selectivity *versus* current density for various $KHCO_3$ concentrations on a flat oxide-derived Cu catalyst. (b) CH_4 selectivity *versus* current density for various $KHCO_3$ concentrations on a flat oxide-derived Cu catalyst. (c) Applied potential for each current density and electrolyte concentration. Predicted (d) local electrode pH and (e) local electrode CO_2 concentration using a diffusion based model and variable-diffusion thickness. The inputted selectivities used to calculate the gas evolved from the electrode and electrons consumed for (d) and (e) are 50% H_2, 30% C_2H_4, 10% CH_4, 5% HCOOH and 5% EtOH.

at low overall current densities (Fig. S6†). As the local electrode pH increases with current density we then expect the onset potential of CH_4 to shift to higher overpotentials while the onset potential of C_2H_4 remains fixed. As current is increased, however, we observe both CH_4 and C_2H_4 production increasing towards a peak selectivity. As seen in Fig. 3a and b, however, as the total current approaches 50 mA cm^{-2} the C_2H_4 partial current density remains relatively constant while CH_4 production greatly decreases. Observing Fig. 3d the drop in CH_4 corresponds to the predicted local pH of 12 at an operating potential of −1.4 V, 300 mV greater than our observed C_2H_4 onset potential of −1.1 V. These results indicate that while CH_4 may be partially suppressed at higher current densities for the Flat electrode at 0.1 M $KHCO_3$, the operating potentials needed to obtain a higher local pH (*via* current density) is misaligned with what would be required to achieve a significant ratio of C_2H_4/CH_4. In the elevated electrolyte concentrations our simulations show that the current densities needed to reach high local pH conditions also do not sufficiently align with the required applied potentials to meaningfully suppress CH_4 production. Furthermore, as seen in Fig. 3c, higher buffering concentrations result in overall more active catalysts for both H_2 and CH_4 formation due to an increased concentration of proton donors.[34] Higher buffering further lowers polarization losses due to pH gradients contributing to more efficient overall reactions.[26]

Of additional interest is the predicted local CO_2 concentration of the Flat samples as a function of current density

and buffering capacity. As seen in Fig. 3e at 0.1 M $KHCO_3$ concentrations the system is expected to become CO_2 limited at 90 mA cm^{-2} for the prescribed selectivity distribution; at higher $KHCO_3$ concentrations this limiting CO_2RR current density increases. The simulation results in Fig. 3e then indicate that the availability of CO_2 is significantly affected by the higher local pH present within the diffusion region at higher currents, despite the relatively slow hydration kinetics of the CO_2 to bicarbonate reaction. Thus while low electrolyte concentrations have experimentally allowed for favorable C_2H_4/CH_4 ratios, the findings in Fig. 3e highlight the necessity of increased buffering concentrations to also obtain significantly higher current densities in fully aqueous reaction systems.

Learning from the limitations of our Flat catalyst, a more energetically efficient catalyst can be used to better align the local electrode pH with the onset potential of C_2H_4. A similar set of experiments to the Flat sample were then undertaken on our electrodeposited oxide-derived Porous catalysts with increased surface roughness and mass transport characteristics. Similar to the Flat sample experiments, gas is collected after 30 minutes of CO_2 reduction, but the selectivity towards C_2H_4 is maintained for at least 45 minutes (a sample test is shown in Fig. S7†). The operating potential also remains stable at the applied current density while minimal change in the morphology is observed before and after CO_2RR (Fig. S4†). As seen in Fig. 4a each of the porous structures result in the peak C_2H_4 selectivity shifting to greater overall current densities.
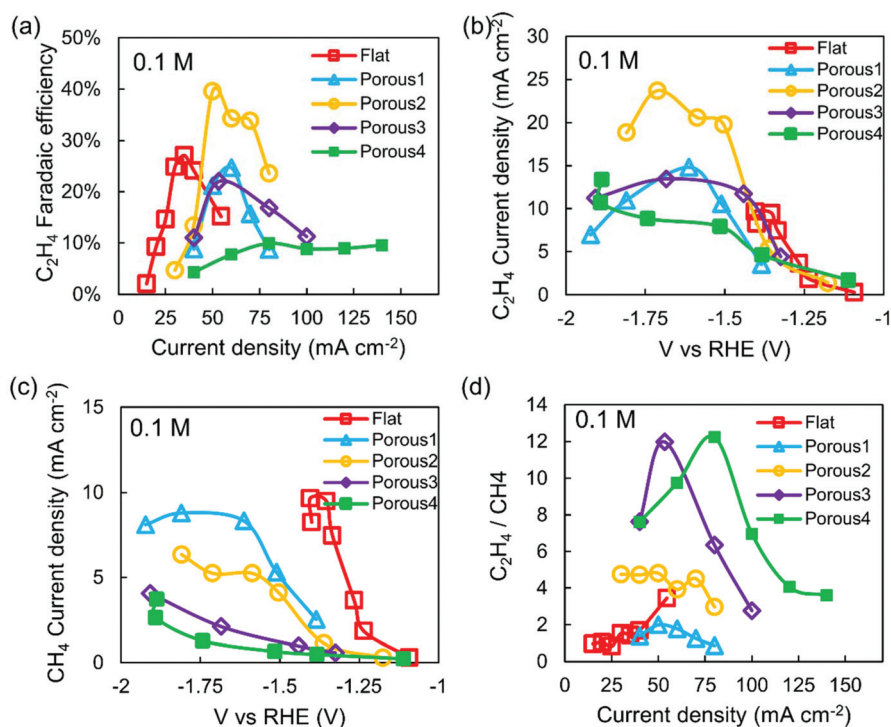

Fig. 4 Impact of mass transportation and electrode surface area on each electrode morphology in 0.1 M $KHCO_3$. (a) C_2H_4 selectivity and (b) C_2H_4 to CH_4 ratio on each catalyst as a function of current densities. (c) CH_4 current density and (d) C_2H_4 current density *versus* applied potential. Solid curves are guides for the eye.

The ratio of C_2H_4/CH_4 product formation similarly increases with Cu deposition time as seen in Fig. 4d with each sample showing multi-fold increases over the Flat sample. The increase is attributed to the decreased overpotentials needed to reach higher currents as seen in Fig. S8† resulting in a higher local pH closer to the onset potential of C_2H_4. As the onset potential of CH_4 production is shifted to higher overpotentials with increasing local pH, electrodes with larger roughness and porosity also allow for favorable C_2H_4 formation over a broader current density range as shown in Fig. 4d. While the Porous 3 and 4 structures exhibit high C_2H_4/CH_4 ratios, the overall C_2H_4 selectivity and current density is low. Similar to the Flat structure we hypothesize this may be due to poor CO_2 availability in the Porous 3 and 4 samples at currents above 50 mA cm^{-2} as calculated from our mass transport model (Fig. 2). Additionally, while our modeling analysis assumes a rough planar electrode, the CO_2 concentration within deeper pores would likely be lower than our predicted value due to a larger overall diffusion thickness from the bottom of the cavity. Thus while higher surface areas from porous materials are shown to be desirable from an energetic efficiency and C_2H_4/CH_4 perspective, they should be balanced with sufficient mass transport to supply the necessary reagent to maintain higher CO_2RR currents. The Faradaic efficiencies are then highly nanostructure-dependent, with both morphology-induced mass transport and surface area influencing the local reaction environment.

Observing the Porous 2 sample, a partial C_2H_4 current of 23 mA cm^{-2} is achieved (Fig. 4b). We attribute the higher selectivity and partial current to the increased mass transport which allows a higher local CO_2 concentration to be maintained at the electrode as current is increased. As shown by Kas *et al.* when increasing system pressure, increased CO_2 availability subsequently increases CO surface coverage. With greater surface coverage of CO the maximum formation rate of C_2H_4 would then be expected to increase,[33,44] highlighting the importance of maintaining ample CO_2 concentration at the electrode surface. For all samples the overall partial C_2H_4 current eventually saturates at higher overpotentials as shown

in Fig. 4b while the selectivity begins to decrease. The Tafel slopes for the target products are shown in Fig. S9.†

From the results of our experiments in 0.1 M KHCO$_3$ and our modeling results in Fig. 3d and e, the electrolyte concentration plays a large role in local pH and CO_2 availability which in turn impacts C_2H_4 production. Previously for the Flat sample increasing buffering resulted in decreased C_2H_4 formation due to a misalignment between the local pH and the onset potential of C_2H_4. For our more electrochemically active Porous samples, however, higher total current densities are possible at lower overpotentials potentially allowing for high buffering capacities to be used, thereby increasing current densities where CO_2 is predicted to become limited. Each of the electrodes were subsequently run at an elevated KHCO$_3$ concentration of 0.2 M with increased overall current densities. The resulting C_2H_4 selectivity curves shown in Fig. 5a mimic a similar overall trend as the 0.1 M KHCO$_3$ tests in Fig. 4a, with the peak selectivity again shifting further to higher current densities in order of increasing deposition time. In the higher buffering environment three of the five samples also reach a C_2H_4 selectivity of ~30% with the Porous 2 and 3 samples achieving a high partial C_2H_4 current of greater than 35 mA cm^{-2}. The best performance, however, belongs to a Porous 2 sample operated in 0.2 M KHCO$_3$ electrolyte concentration using a total current density of 120 mA cm^{-2}, achieving an FE for C_2H_4 of 29.7% and a $j_{C_2H_4}$ of 35.6 mA cm^{-2}, a 3.4-fold increase in C_2H_4 current density as compared to the Flat sample. Additionally all Porous samples exceed their peak partial C_2H_4 current density as compared to the 0.1 M buffering case as seen in Fig. 5c. The increase in partial C_2H_4 current is in contrast to our Flat sample and the findings of Varela *et al.* where the higher buffering is expected to increase the availability of proton donors, increasing reaction kinetics for H_2 and CH_4 formation, but not C_2H_4. We conclude the increased CO_2 availability from the higher electrolyte concentration also increases CO surface coverage increasing CO–CO dimerization and C_2H_4 currents, similar to that found when increasing CO_2 partial pressure by Kas *et al.* Finally, as shown by the simulation in Fig. 3d, the additional buffering capacity
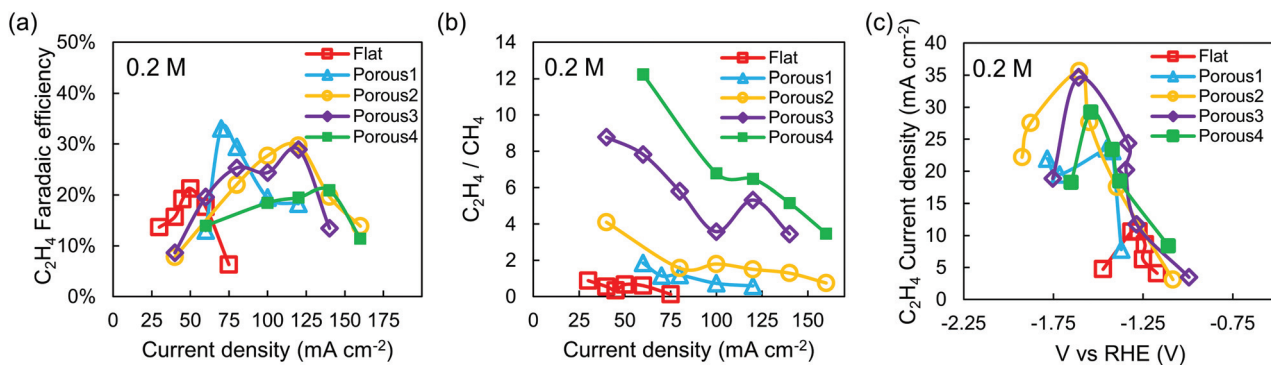

Fig. 5 Impact of mass transportation and electrode surface area on each electrode morphology in 0.2 M KHCO$_3$. (a) Ethylene selectivity and (b) ethylene to methane ratio on each catalyst morphology as a function of current densities. (c) Ethylene current density *versus* applied potential. Solid curves are guides for the eye.

also requires a higher current density to reach a higher local pH which explains the observed shift in peak C_2H_4 selectivity to higher current densities.

From our results several important trends are extracted. The first is in regards to the importance of increasing surface roughness to drive CO_2 product formation towards C2 products rather than CH_4. Under both 0.1 M and 0.2 M electrolyte concentrations higher C_2H_4/CH_4 ratios were obtained with increasing electrode roughness and porosity as higher currents are observed at lower overpotentials. Heightened local pH values can then occur closer to the observed onset potential of C_2H_4, suppressing CH_4. Secondly, our experimental and modeling results indicate that CO_2 limitations occur as a result of operating under high local pH conditions, affecting maximum CO_2RR production rates. While surface-derived mass transport effects can partially mitigate pH-driven CO_2 limitations, as illustrated by the performance of the Porous 2 sample, substantial increases in C_2H_4 current densities requires an increase in the electrolyte buffering capacity. Finally, while higher electrolyte concentrations are fundamentally needed to achieve higher efficiencies and production rates of C_2H_4, increasing the concentration of HCO_3^- can provide too strong a buffering affect to take advantage of separating the onset potentials of C_2H_4 and CH_4. Additionally, the increased proton availability can facilitate competing H_2 and CH_4 reactions.

Maximizing the performance of C_2H_4 production on oxide-derived Cu then requires a number of contending factors to be taken into consideration including operating potential, CO_2 availability and catalyst activity. Under aqueous H-cell configurations C_2H_4 production will then always be confined to a narrow operating region where C_2H_4 is most favorable before either competing reactions take over or the CO_2 reagent is depleted by consumption or pH-driven conversion into carbonate. For efficient C_2H_4 production it is then necessary to design catalysts and systems that enable decoupling of these underlying factors to provide further degrees of freedom to increase selectivity and current density concurrently. Catalytically this requires further pH-independent separation of C_2H_4 and CH_4 onset potentials through material design and a better understanding of individual reaction mechanisms through theoretical studies. System-based approaches, such as flow cell devices, can also be used which allows for catalysts to operate in a high pH media with ample CO_2, providing a much broader current range where optimal reaction conditions can exist.[45,46]

Conclusion

In this work we assessed the potential of increasing the partial current density of C_2H_4 on oxide-derived Cu within an H-cell configuration. By creating electrodes with varying surface areas and mass transport properties we were able to increase the C_2H_4 partial current to 35.6 mA cm^{-2} on our Porous 2 sample, a 3.4-fold increase over the Flat comparison. Highlighted by

our experiments are the fundamental constraints of C_2H_4 production on a Cu-oxide derived catalyst due to the coupled effects of the applied potential on current density and local pH. When poorly aligned, low C_2H_4/CH_4 ratios are observed while operating under high local pH conditions are shown to additionally constrain CO_2 availability, hindering maximum current densities. We hope the combined material and mass transport analysis presented aids in disentangling the competing influences of CO_2 reduction on Cu-based catalysts and that similar methods can be used in the testing of newly discovered catalysts in the future.

Experimental section

Cu foil substrates with a 99.9% purity were purchased from Sigma Aldrich. Cu foil was cleaned prior to wet oxidation or electrodeposition. The sample was first sonicated in 3 M HCl for 10 minutes, and then sonicated in isopropanol for 10 minutes. The samples were rinsed with deionized water and dried in a flowing nitrogen gas stream following each of the cleaning steps. All samples used in this work had a working area of 0.09 cm^2.

Electrodeposition of a Cu foam structure was performed as described previously.[47] Briefly, a two-electrode system in an 80 mL beaker was used for the deposition process. The working electrode (substrate for deposition) and the counter electrode were both Cu foil (99.9% purity, Sigma Aldrich). A precursor solution that consists of 0.2 M $CuSO_4$, 0.7 M H_2SO_4, and 1.2 M $(NH_4)_2SO_4$ was used. An electrochemical workstation (Autolab PGSTAT204) running in galvanostatic mode at a current density of 3 A cm^{-2} was used for the deposition, and deposition duration was varied and specified accordingly in the main text.

Wet oxidation of the Cu samples was performed as follows. Cleaned flat Cu foils or electrodeposited Cu foam samples were immersed into an oxidant solution consisting of 60 mM HCl (Sigma Aldrich) and 60 mM H_2O_2 (Sigma Aldrich) without stirring for 60 seconds. The samples were immediately rinsed in deionized water and dried again in a flowing nitrogen gas stream.

The electrochemically active surface area was assessed by capacitance measurements with different scan rates as shown in Fig. S1.† [48] CV scans are performed in 0.1 M $KHCO_3$ saturated with CO_2. The change in electrochemically active surface area was additionally assessed by the under potential deposition of Pb (Fig. S2†).[49] An aqueous electrolyte containing 0.01 M $Pb(NO_3)_2$ and 0.1 M HCl was used.

The composition of the nanoparticles formed on the Cu foil substrate after wet-oxidation were observed by X-ray diffraction (XRD) in Fig. S10.† X-ray photoelectron spectroscopy (XPS) were performed for each of the flat and porous samples before and after CO_2RR as shown in Fig. S3.† The spectra before CO_2RR show a Cu 2p3/2 peak of 932.41 ± 0.1 eV and after CO_2RR a reduced peak of 932.15 ± 0.08 eV. The XRD pattern of the sample after wet-oxidation shows primarily Cu(I) oxide

present on the Cu substrate with minor amounts of Cu(II) oxides also present.

An Autolab PGSTAT204 electrochemical workstation was used for all electrochemical processes described in this work with new samples used for each data point. The electrochemical workstation was run in galvanostatic mode at various current densities and product gases were collected after running for 30 min at the prescribed current. Gas product detection was performed using a PerkinElmer Clarus 680 gas chromatography system. For the Porous 2 sample the experiments were also run in potentiostatic mode at the same potentials found from the galvanostatic setup. The resulting current densities are found to agree with the prescribed currents as seen in Fig. S11.†

All CO_2 reduction experiments were performed in a three-electrode system connected to the electrochemical workstation. An Ag/AgCl (with saturated KCl as the filling solution) and platinum foil were used as reference and counter electrodes, respectively. Electrode potentials were converted to the reversible hydrogen electrode (RHE) reference scale using $E_{RHE} = E_{Ag/AgCl} + 0.197$ V $+ 0.0591 \times$ pH. The $KHCO_3$ electrolytes with concentrations 0.1 M, 0.2 M, 0.3 M and 0.5 M saturated with CO_2 have pH values of 6.8, 6.9, 7.0 and 7.2, respectively. The experiments were performed in a gas-tight two-compartment H-cell separated by an ion exchange membrane (Nafion117). 30 mL of electrolyte was used in both the anode and cathode sides, and the gas phase headspace in both the anode and cathode sides was approximately 20 mL. The electrolyte in the cathodic compartment was stirred at a rate of 500 rpm during electrolysis. CO_2 gas (99.99%, Praxair) was delivered into the cathodic compartment at a rate of 20.00 standard cubic centimeters per minute (s.c.c.m.) and was routed into a gas chromatograph (PerkinElmer Clarus 680). The gas chromatograph was equipped with a Molecular Sieve 5A capillary column and a packed Carboxen-1000 column. Argon (Linde, 99.999%) was used as the carrier gas. The gas chromatograph columns led directly to a thermal conductivity detector to quantify hydrogen, and a flame ionization detector equipped with a methanizer to quantify methane and ethylene.

Bubble release diameters were determined by visual observation of gas evolution from each of the three primary electrode surfaces: flat copper, oxidized Cu with short deposition time and oxidized copper with longer deposition (Cu foam structure). Bubble diameters were recorded at the time of release from a horizontal electrode surface witnessed from above using a dark-field microscope similar to our previous publication.[41]

Notes and references

1 D. D. Zhu, J. L. Liu and S. Z. Qiao, *Adv. Mater.*, 2016, **28**, 3423–3452.
2 P. Kumar, A. Bansiwal, N. Labhsetwar and S. L. Jain, *Green Chem.*, 2015, **17**, 1605–1609.
3 T. Wu, L. Zou, D. Han, F. Li, Q. Zhang and L. Niu, *Green Chem.*, 2014, **16**, 2142–2146.
4 X. Li, J. Wen, J. Low, Y. Fang and J. Yu, *Sci. China Mater.*, 2014, **57**, 70.
5 D. H. Won, H. Shin, J. Koh, J. Chung, H. S. Lee, H. Kim and S. I. Woo, *Angew. Chem., Int. Ed.*, 2016, **55**, 9297–9300.
6 M. Ma, B. J. Trześniewski, J. Xie and W. A. Smith, *Angew. Chem., Int. Ed.*, 2016, **55**, 9748–9752.
7 M. Liu, Y. Pang, B. Zhang, P. De Luna, O. Voznyy, J. Xu, X. Zheng, C. T. Dinh, F. Fan, C. Cao, F. P. G. de Arquer, T. S. Safaei, A. Mepham, A. Klinkova, E. Kumacheva, T. Filleter, D. Sinton, S. O. Kelley and E. H. Sargent, *Nature*, 2016, **537**, 382–386.
8 A. S. Varela, W. Ju, T. Reier and P. Strasser, *ACS Catal.*, 2016, **6**, 2136–2144.
9 S. Gao, X. Jiao, Z. Sun, W. Zhang, Y. Sun, C. Wang, Q. Hu, X. Zu, F. Yang, S. Yang, L. Liang, J. Wu and Y. Xie, *Angew. Chem., Int. Ed.*, 2016, **55**, 698–702.
10 Y. Wang, J. Zhou, W. Lv, H. Fang and W. Wang, *Appl. Surf. Sci.*, 2016, **362**, 394–398.
11 X. Sun, Q. Zhu, X. Kang, H. Liu, Q. Qian, Z. Zhang and B. Han, *Angew. Chem., Int. Ed.*, 2016, **55**, 6771–6775.
12 H. Mistry, A. S. Varela, C. S. Bonifacio, I. Zegkinoglou, I. Sinev, Y.-W. Choi, K. Kisslinger, E. A. Stach, J. C. Yang, P. Strasser and B. R. Cuenya, *Nat. Commun.*, 2016, **7**, 12123.
13 F. S. Roberts, K. P. Kuhl and A. Nilsson, *Angew. Chem., Int. Ed.*, 2015, **54**, 5179–5182.
14 J. Wu, S. Ma, J. Sun, J. I. Gold, C. Tiwary, B. Kim, L. Zhu, N. Chopra, I. N. Odeh, R. Vajtai, A. Z. Yu, R. Luo, J. Lou, G. Ding, P. J. A. Kenis and P. M. Ajayan, *Nat. Commun.*, 2016, **7**, 13869.
15 A. D. Handoko, C. W. Ong, Y. Huang, Z. G. Lee, L. Lin, G. B. Panetti and B. S. Yeo, *J. Phys. Chem. C*, 2016, **120**, 20058–20067.
16 D. Ren, Y. Deng, A. D. Handoko, C. S. Chen, S. Malkhandi and B. S. Yeo, *ACS Catal.*, 2015, **5**, 2814–2821.
17 S. Lee, D. Kim and J. Lee, *Angew. Chem., Int. Ed.*, 2015, **127**, 14914–14918.
18 R. Kas, R. Kortlever, A. Milbrat, M. T. M. Koper, G. Mul and J. Baltrusaitis, *Phys. Chem. Chem. Phys.*, 2014, **16**, 12194–12201.

19 D. Gao, I. Zegkinoglou, N. J. Divins, F. Scholten, I. Sinev, P. Grosse and B. Roldan Cuenya, *ACS Nano*, 2017, **11**, 4825–4831.

20 W. Tang, A. A. Peterson, A. S. Varela, Z. P. Jovanov, L. Bech, W. J. Durand, S. Dahl, J. K. Nørskov and I. Chorkendorff, *Phys. Chem. Chem. Phys.*, 2011, **14**, 76–81.

21 O. A. Baturina, Q. Lu, M. A. Padilla, L. Xin, W. Li, A. Serov, K. Artyushkova, P. Atanassov, F. Xu, A. Epshteyn, T. Brintlinger, M. Schuette and G. E. Collins, *ACS Catal.*, 2014, **4**, 3682–3695.

22 A. Loiudice, P. Lobaccaro, E. A. Kamali, T. Thao, B. H. Huang, J. W. Ager and R. Buonsanti, *Angew. Chem., Int. Ed.*, 2016, **55**, 5789–5792.

23 M. Ma, K. Djanashvili and W. A. Smith, *Angew. Chem., Int. Ed.*, 2016, **55**, 6680–6684.

24 D. Raciti, K. J. Livi and C. Wang, *Nano Lett.*, 2015, **15**, 6829–6835.

25 N. Gupta, M. Gattrell and B. MacDougall, *J. Appl. Electrochem.*, 2005, **36**, 161–172.

26 M. R. Singh, E. L. Clark and A. T. Bell, *Phys. Chem. Chem. Phys.*, 2015, **17**, 18924–18936.

27 R. Kortlever, J. Shen, K. J. P. Schouten, F. Calle-Vallejo and M. T. M. Koper, *J. Phys. Chem. Lett.*, 2015, **6**, 4073–4082.

28 K. D. Yang, W. R. Ko, J. H. Lee, S. J. Kim, H. Lee, M. H. Lee and K. T. Nam, *Angew. Chem., Int. Ed.*, 2017, **56**, 796–800.

29 A. Dutta, M. Rahaman, N. C. Luedi, M. Mohos and P. Broekmann, *ACS Catal.*, 2016, **6**, 3804–3814.

30 S. Sen, D. Liu and G. T. R. Palmore, *ACS Catal.*, 2014, **4**, 3091–3095.

31 A. S. Hall, Y. Yoon, A. Wuttig and Y. Surendranath, *J. Am. Chem. Soc.*, 2015, **137**, 14834–14837.

32 R. Kas, R. Kortlever, H. Yılmaz, M. T. M. Koper and G. Mul, *ChemElectroChem*, 2015, **2**, 354–358.

33 J. H. Montoya, C. Shi, K. Chan and J. K. Nørskov, *J. Phys. Chem. Lett.*, 2015, **6**, 2032–2037.

34 A. S. Varela, M. Kroschel, T. Reier and P. Strasser, *Catal. Today*, 2016, **260**, 8–13.

35 H. Xiao, T. Cheng, W. A. Goddard and R. Sundararaman, *J. Am. Chem. Soc.*, 2016, **138**, 483–486.

36 K. J. P. Schouten, E. Pérez Gallent and M. T. M. Koper, *J. Electroanal. Chem.*, 2014, **716**, 53–57.

37 H.-C. Shin, J. Dong and M. Liu, *Adv. Mater.*, 2003, **15**, 1610–1614.

38 C. W. Li and M. W. Kanan, *J. Am. Chem. Soc.*, 2012, **134**, 7231–7234.

39 C. W. Li, J. Ciston and M. W. Kanan, *Nature*, 2014, **508**, 504–507.

40 H. Xiao, W. A. Goddard, T. Cheng and Y. Liu, *Proc. Natl. Acad. Sci. U. S. A.*, 2017, **114**, 6685–6688.

41 T. Burdyny, P. J. Graham, Y. Pang, C.-T. Dinh, M. Liu, E. H. Sargent and D. Sinton, *ACS Sustainable Chem. Eng.*, 2017, **5**, 4031–4040.

42 C. a. C. Sequeira, D. M. F. Santos, B. Šljukić and L. Amaral, *Braz. J. Phys.*, 2013, **43**, 199–208.

43 P. Lobaccaro, M. R. Singh, E. L. Clark, Y. Kwon, A. T. Bell and J. W. Ager, *Phys. Chem. Chem. Phys.*, 2016, **18**, 26777–26785.

44 Y. Yang, P. Cheng, S. Zhang and S. Huang, *RSC Adv.*, 2016, **6**, 4354–4364.

45 S. Ma, M. Sadakiyo, R. Luo, M. Heima, M. Yamauchi and P. J. A. Kenis, *J. Power Sources*, 2016, **301**, 219–228.

46 C. Reller, R. Krause, E. Volkova, B. Schmid, S. Neubauer, A. Rucki, M. Schuster and G. Schmid, *Adv. Energy Mater.*, 2017, **7**, 1602114.

47 D. Nam, R. Kim, D. Han, J. Kim and H. Kwon, *Electrochim. Acta*, 2011, **56**, 9397–9405.

48 S. Ma, Q. Zhu, Z. Zheng, W. Wang and D. Chen, *Chem. Commun.*, 2015, **51**, 15815–15818.

49 T. Pounds, K. Sieradzki, J. Erlebacher and R. C. Cammarata, *J. Electrochem. Soc.*, 2017, **164**, D307–D314.